ARTICLE

BIOTECHNOLOGY and BIOENGINEERING

Assessing the Influence of Biofilm Surface Roughness on Mass Transfer by Combining Optical Coherence Tomography and Two-Dimensional Modeling

Chunyan Li,[1] Michael Wagner,[1,2] Susanne Lackner,[1,3] Harald Horn[1]

[1]Chair of Water Chemistry, Water Technology, Karlsruhe Institute of Technology, Engler-Bunte-Ring 9, Karlsruhe 76131, Germany; telephone: +49 72160842580; fax: +49 72160846497; e-mail: harald.horn@kit.edu

[2]Institute of Functional Interfaces, Karlsruhe Institute of Technology, Eggenstein-Leopoldshafen, Germany

[3]Urban Bioengineering for Resource Recovery, Bauhaus-Institute for Infrastructure Solutions, Bauhaus-Universityät Weimar, Weimar, Germany

ABSTRACT: Imaging and modeling are two major approaches in biofilm research to understand the physical and biochemical processes involved in biofilm development. However, they are often used separately. In this study we combined these two approaches to investigate substrate mass transfer and mass flux. Cross-sectional biofilm images were acquired by means of optical coherence tomography (OCT) for biofilms grown on carriers. A 2D biofilm model was developed incorporating OCT images as well as a simplified biofilm geometry serving as structural templates. The model incorporated fluid flow, substrate transfer and biochemical conversion of substrates and simulated the hydrodynamics surrounding the biofilm structure as well as the substrate distribution. The method allowed detailed analysis of the hydrodynamics and mass transfer characteristics at the micro-scale. Biofilm activity with respect to substrate fluxes was compared among different combinations of flow, substrate availability and biomass density. The combined approach revealed that higher substrate fluxes at heterogeneous biofilm surface under two conditions: pure diffusion and when high flow velocity along the biofilms surface renders the whole liquid-biofilm interface to be highly active. In-between the two conditions the substrate fluxes across the surface of smooth biofilm geometry were higher than that of the heterogeneous biofilms.

Biotechnol. Bioeng. 2016;113: 989–1000.

KEYWORDS: biofilm imaging; optical coherence tomography; biofilm modeling; mass transfer; convection; diffusion

Introduction

When microorganisms attach to surfaces in an aquatic environment, they form biofilms, the dominating style of microbial life on Earth. Determining biofilm structure is of great importance in biofilm research, as it is known to have strong impact on biofilm activity (Picioreanu et al., 2000).

As one of the major approaches in biofilm research, mathematical modeling has become one of the essential tools to gain mechanistic understanding of systems with complex interactions (Horn and Lackner, 2014). A planar biofilm structure is often assumed in simplified one-dimensional (1D) models, as in the widely used one from Wanner and Reichert (1996). This assumption limits the applicability of such models when biofilm surface heterogeneity is important and required as input. Multi-dimensional models can incorporate the spatial heterogeneity of biofilm structure and can provide insights into the spatial distribution of state variables (e.g., gradients in substrates and biomass concentration) (Picioreanu et al., 2004) and the structure-activity relationship by applying conditions close to reality (Eberl et al., 2000). So far, the microbial components in biofilms can be described with the following approaches: cellular automata (CA) (Laspidou and Rittmann, 2004), individual-based models (Kreft et al., 2001), particle-based models (Picioreanu et al., 2004) and the continuum approach (Alpkvist and Klapper, 2007). Even with the simplifications that have to be made, the quantitative nature of a biofilm model provides details on a conceptual understanding and allows a rigorous evaluation of this understanding against experimental results.

In another branch of biofilm research, various imaging techniques have been applied to investigate the structure and composition of biofilms, such as confocal laser scanning microscopy (CLSM) (Lawrence and Neu, 1999), magnetic resonance imaging (MRI)

Correspondence to: H. Horn
Received 13 July 2015; Revision received 13 October 2015; Accepted 19 October 2015
Accepted manuscript online 24 October 2015;
Article first published online 10 November 2015 in Wiley Online Library (http://onlinelibrary.wiley.com/doi/10.1002/bit.25868/abstract).
DOI 10.1002/bit.25868

(Manz et al., 2003), raman microscopy (RM) (Ivleva et al., 2009) and scanning electron microscopy (SEM) (Janjaroen et al., 2013). However, their application is limited due to incomplete staining of biofilm constitutes (CLSM) or altering the biofilm structure due to drying (SEM), not being representative due to imaging at micro-scale (CLSM, SEM) or high costs for instrumentation and time (MRI).

Originally invented for medical diagnostics (Huang et al., 1991), optical coherence tomography (OCT) has recently been introduced into biofilm research to reliably monitor biofilm development at mm-scale (meso-scale) (Wagner et al., 2010; Xi et al., 2006). It compensates the aforementioned limitations and enables fast, in situ and non-invasive three-dimensional visualization of biofilm structure at the meso-scale and thus exhibits high potential in biofilm research.

Typically, biofilm imaging and mathematical modeling are used separately. There have very seldom been interactions between the two approaches (Böl et al., 2009; Pavissich et al., 2014). Within this study, we developed a method that combines biofilm imaging at the meso-scale by means of OCT with the purpose of using the imaging data as structural templates within a 2D biofilm model to assess the impact of biofilm structure on local mass transfer. Comparison between real biofilm structures and a smooth biofilm structure was conducted to investigate the impact of biofilm surface heterogeneity.

Materials and Methods

Biofilm Imaging

The biofilm samples for the current study were grown in a biofilm reactor using plastic carriers (see Fig. 1, prototype from AnoxKaldnes) as substratum. The reactor was operated with glucose ($\sim$10 [g/($m^2 \cdot$ d)]) as the only carbon source and dissolved oxygen (DO) at around 7.5 mg/L (Details on reactor operation are provided in the supplementary material). A GANYMEDE spectral domain OCT (Thorlabs GmbH, Dachau, Germany) with a central wavelength of 930 nm was used to visualize the biofilm structure. For image acquisition the carrier was placed in an in-house made carrier holder and immersed into filtered ($<$0.45 μm) bulk liquid from the reactor. The image spanned two compartments in width. The images have a lateral resolution of 10.7 μm/pixel (in x-direction) and an axial resolution of 2.09 μm/pixel (in z-direction).

Image Analysis and Characterization of Biofilm Structure

Image processing was conducted using Fiji software package (Schindelin et al., 2012). The complete biofilm structure throughout the vertical cross-section of the carrier was achieved by combining two B-scans acquired at the same location (marked in Fig. 1) from both sides of the carrier, with each B-scan contributing 50% of the carrier thickness. After binarization by setting a manual threshold (Yang et al., 2001), the surface of the biofilm was clearly identifiable. Noise pixels and isolated pixel groups were removed with the "Remove outlier" function of Fiji. Compact biofilm was assumed, thus the space beneath the biofilm surface was treated as completely filled with biomass. In the last step the plastic grids of the carrier were outlined and removed from the images to allow the model to distinguish between the plastic carrier and the grown biofilm.

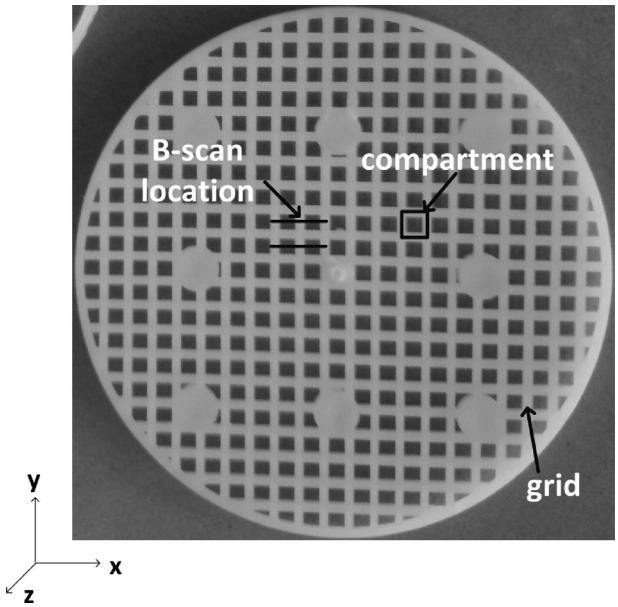

Figure 1. Photograph of the carrier used for biofilm cultivation. The carrier has a dimension of 3 mm in diameter and 1.05 mm in thickness. A compartment refers to one small hole on the carrier. The compartment size is 1.4 × 1.4 mm^2. The two black lines indicate where the B-scans for the simulation were taken. The optical axis z refers to the direction perpendicular to the carrier surface.

Based on the binarized images, biofilm structures were characterized with respect to roughness coefficient (R'_a) (Derlon et al., 2012; Murga et al., 1995) and surface enlargement factor (α) (Picioreanu et al., 1998), calculated according to Equations 1 and 2, respectively.

$$R'_a = \frac{1}{N}\sum_1^N \left(\frac{|L_{f,i} - \overline{L_f}|}{\overline{L_f}} \right) \quad (1)$$

$$\alpha = \frac{L_\Gamma}{L_S} \quad (2)$$

where $L_{f,i}$ is the biofilm thickness at point i on the discretized biofilm surface, $\overline{L_f}$ the average biofilm thickness, N the number of points engaged in the calculation, L_Γ the measured length of the liquid–biofilm interface, L_S the length of the substratum.

Model Structure

Biofilm geometries were created based on the binarized OCT images using the "mphimage2geom" function provided by COMSOL LiveLink for Matlab. Afterwards, the simulations were conducted in COMSOL Multiphysics 4.4 (COMSOL Inc., Sweden). Fluid flow, mass transport and biochemical conversion of substrates under steady state flow conditions were incorporated into the model. For simplicity reasons the flow in the space close to the carrier surface was assumed stationary and incompressible. Flow, both parallel to the carrier surface and through the compartments, was simulated.

The simulation domain was extended by 1.5 mm above as well as below the carrier surface to allow incorporating a fully developed flow field. Based on this adjustment, the motion of the liquid in the simulation domain can be characterized by the velocity field **u**, which is governed by the Navier-Stokes equations:

$$\rho(\boldsymbol{u}\cdot\nabla)\boldsymbol{u} = -\nabla P + \mu\nabla^2\boldsymbol{u} \tag{3}$$

$$\nabla\cdot\boldsymbol{u} = 0 \tag{4}$$

where Equation 3 is the balance of inertial, pressure and viscous forces, and Equation 4 describes the incompressibility-induced mass balance. **u** is the vector of the local liquid velocity, rho is the liquid density, μ is the liquid dynamic viscosity and P stands for pressure. Specification of boundary conditions for both parallel flow and flow through conditions was given in Figure 2.

Biofilm was assumed rigid. Dissolved components include organic substrates characterized by the chemical oxygen demand (COD) and dissolved oxygen (DO). Transport of dissolved components in the liquid and biofilm domain by convection and diffusion was described by Equation 5:

$$\nabla\cdot(-D_i\nabla S_i) + \boldsymbol{u}\cdot\nabla S_i = r_i \tag{5}$$

where D_i is the diffusivity of substrate i, S_i the concentration of substrate i in the liquid and biofilm domain and r_i the turnover of substrate i in biofilm domain. The diffusivity of substrates within biofilms was assumed to equal 80% of that in the bulk liquid (Horn and Morgenroth, 2006; Stewart, 2003).

Substrate flux is continuous at the liquid-biofilm interface. The COD (148 mg/L) concentration in the bulk liquid measured on the day when the images were taken was used for all the simulations. Substrate conversion was only considered in the biofilm domain. Aerobic conversion of COD by heterotrophic bacteria followed a dual Monod kinetic (Henze, 2000) and is given by Equation 6 and 7, respectively.

$$r_{\mathrm{COD}} = -\frac{1}{Y_H}\mu_H\left(\frac{S_{\mathrm{COD}}}{K_{\mathrm{COD}}+S_{\mathrm{COD}}}\right)\left(\frac{S_{\mathrm{DO}}}{K_{\mathrm{DO}}+S_{\mathrm{DO}}}\right)X_H \tag{6}$$

$$r_{\mathrm{DO}} = -\frac{1-Y_H}{Y_H}\mu_H\left(\frac{S_{\mathrm{COD}}}{K_{\mathrm{COD}}+S_{\mathrm{COD}}}\right)\left(\frac{S_{\mathrm{DO}}}{K_{\mathrm{DO}}+S_{\mathrm{DO}}}\right)X_H \tag{7}$$

The values for all stoichiometric and kinetic parameters were set according to the Activated Sludge Model No.1 (Henze, 2000) and are provided in Table I. Growth and inactivation of microorganisms were not considered within this study. Biomass density was defined as only for the active biomass homogeneously distributed over the entire biofilm domain. Two values, low (15,000 g/m^3) and high (30,000 g/m^3) biomass density (Wäsche et al., 2002), were used for the simulation.

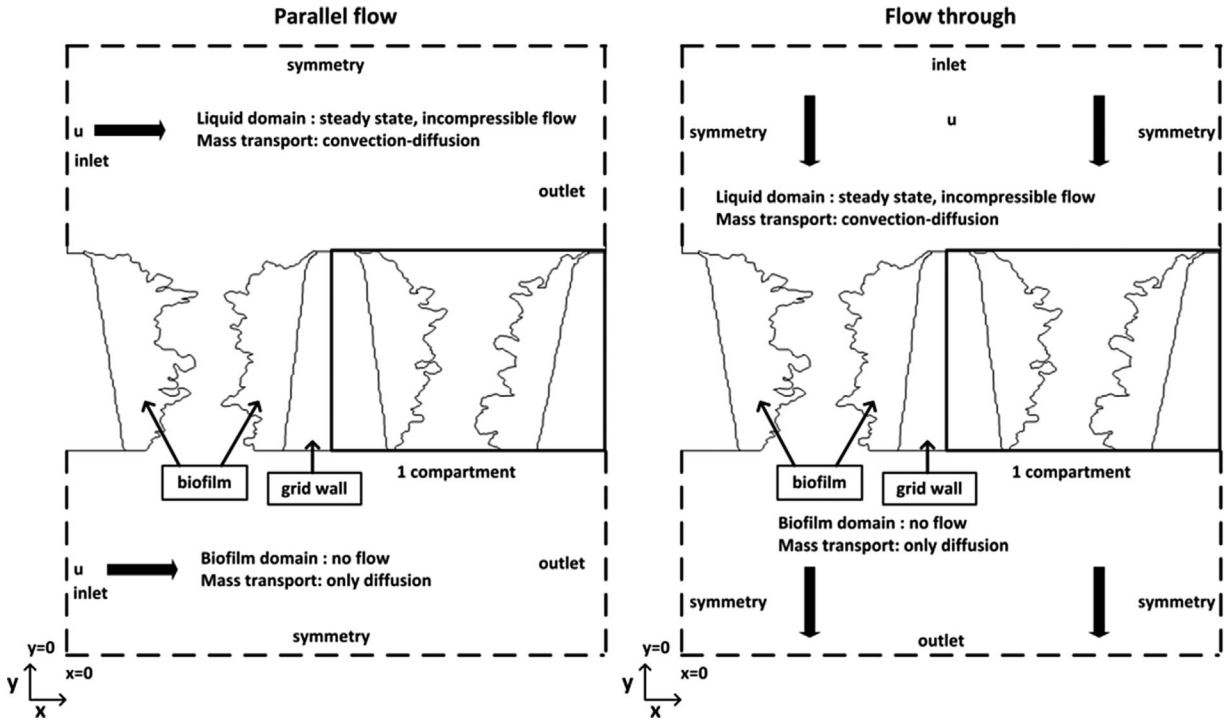

Figure 2. Model structure and specifications for boundary condition for both parallel and flow throughconditions. The dimension of the simulation domain is 2.8 × 4.05 mm^2. The black rectangular bounds a compartment.

Table I. Model parameters.

Symbol	Value	Dimension	Description	Reference
Stoichiometric parameter				
Y_H	0.67	$gCOD \cdot gCOD^{-1}$	Heterotrophic yield coefficient on substrate	Henze (2000)
Kinetic parameters				
μ_H	6	d^{-1}	Maximum specific growth rate of biomass	Henze (2000)
K_S	20	$gCOD \cdot m^{-3}$	Half-saturation coefficient for substrate S	Henze (2000)
K_{DO}	0.2	$gO_2 \cdot m^{-3}$	Half-saturation coefficient for oxygen	Henze (2000)
Additional parameters				
D_{COD}	$1.2 \times 10{-}9$	$m^2 \cdot s^{-1}$	Diffusivity of COD in water	Lide (2003)
D_{DO}	$2.0 \times 1{-}9$	$m^2 \cdot s^{-1}$	Diffusivity of DO in water	Lide (2003)

Data Evaluation

The conversion of organic substrate was evaluated as the average COD flux over the substratum according to Fick's law:

$$J_{COD} = \frac{\int -D_{COD} \frac{\partial S_{COD}}{\partial n}|_{\Gamma}}{L_s} \tag{8}$$

where Γ refers to the biofilm surface. L_S equals the length of the substratum. n indicates the direction normal to the biofilm surface at local position.

The local convective and diffusive fluxes were calculated based on Equation 9 and 10, respectively for the whole simulation domain.

$$J_C = S_{COD}\sqrt{u_x^2 + u_y^2} \tag{9}$$

$$J_D = D_{COD}\sqrt{\left(\frac{\partial S_{COD}}{\partial x}\right)^2 + \left(\frac{\partial S_{COD}}{\partial y}\right)^2} \tag{10}$$

The Sherwood number (Sh) is a dimensionless number used to characterize the mass transfer characteristics and represents the ratio of convective to diffusive mass transport (Picioreanu et al., 2000; Taherzadeh et al., 2012). For a given system, the higher the Sh, the better the mass transfer from the liquid into the biofilms. The locally resolved Sherwood number can be calculated according to Equation 11:

$$Sh = \frac{k_S L_h}{D_S} = \frac{-L_h \frac{\partial S_{O2}}{\partial n}|_{\Gamma}}{S_{O2,0} - S_{O2,\tau}} \tag{11}$$

where $S_{i,0}$ and $S_{i,\tau}$ denote the DO concentration in the inflow and at one point on biofilm surface.

The characteristic length (L_h) was chosen to be the width of the simulation domain, 2.8 mm. To compare the mass transfer characteristic among different simulations, the spatially averaged Sherwood number ($\overline{Sh}$) was calculated by averaging Sh over biofilm surface Γ as given in Equation 12:

$$\overline{Sh} = \frac{\int_{\Gamma} Sh \cdot d_{\Gamma}}{L_{\Gamma}} \tag{12}$$

Results

Biofilm Images Obtained With OCT

The structure of biofilms on carriers was obtained by means of OCT. Two cross-sectional OCT images, referred to as geometry 1 (G1) and geometry 2 (G2), are presented in Figure 3a and b. The two geometries differed slightly with respect to L_{Γ}, R'_a, and α, see Table II. Heterogeneous structures with small spikes developed along the carrier walls, which can be clearly seen from the binarized images in Figure 3c and d.

A simplified smooth geometry was generated (see Fig. 3e) to study the impact of biofilm surface heterogeneity. The smooth geometry had the average biofilm area of G1 and G2 (see Table II). However, there was a distinctive difference with respect to the liquid–biofilm interface length (L_{Γ}) as well as biomass distribution between the real and the simplified structures. Compared to the flat geometry, the heterogeneous biofilm structure doubled L_{Γ} (see Table II). With the same substratum length, the presence of spikes in the real biofilm structure enlarged the biofilm surface, namely L_{Γ}. This further led to a high R'_a and α.

Simulated Velocity and Concentration Fields

To demonstrate the applicability of the method combining biofilm imaging and biofilm modeling, geometries were transferred into COMSOL to serve as structural templates, which allowed studying the interaction between the biofilm structure and the surrounding fluid. The simulated flow field in the vicinity of and inside the two adjacent compartments (G1) is presented in Figure 4a. Figure 4b presents the simulated flow field around the simplified biofilm structure under the same simulation conditions. The streamlines clearly depict the formation of (laminar) recirculation zone inside the carrier compartments for both biofilm geometries. From red to blue color, the figure shows that fluid velocity decreases from 8 cm/s to 0 near the biofilm surface.

The convective and diffusive transport of substrates was coupled to the flow simulation. Figure 4c and d present the simulated distribution of DO in the liquid and in the biofilm matrix. The figures show that DO concentration decreased steadily from 8 mg/L at biofilm surface to less than 1 mg/L near the plastic of the carrier and became limited in the deeper layer of the biofilm. The green color inside the compartments in Figure 4c suggests that liquid could not flow through the compartments, thereby forming

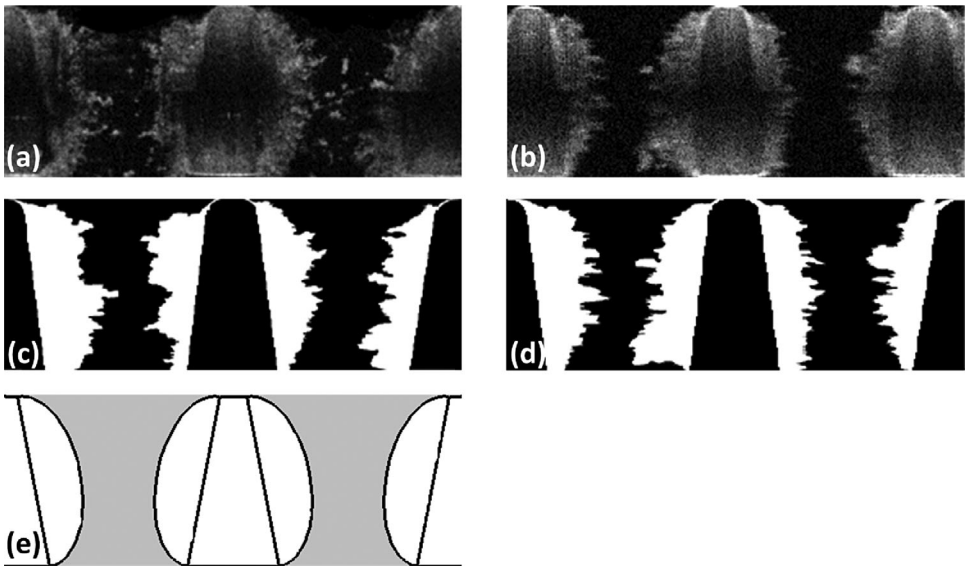

Figure 3. Cross-sectional OCT images of biofilm developed on the carrier. (**a**) geometry 1 and (**b**) geometry 2 are raw gray scale biofilm images. (**c**) and (**d**) are the binarized images for (**a**) and (**b**) respectively. (**e**) presents the simplified biofilm structure that has the average area of (**c**) and (**d**). The dimension of one image is $2.8 \times 1.05\ mm^2$ and represents a cross section through two compartments in the vertical xz-plane.

diffusion-dominated regions. Whereas in the simulation presented in Figure 4d the liquid flew through the compartments and transported the substrate deep into the compartments. COD concentration fields exhibit the same pattern for the corresponding geometry (see Figure S1).

The activity of the biomass with respect to COD consumption, calculated based on Equation 6, is visualized in Figure 4e and f for G1 and the simplified structure, respectively. Biofilms reached the highest activity of $1.34\ g/(m^3 \cdot s)$ at the biofilm surface where the substrates were not limited. Away from the biofilm surface, biomass activity decreased steadily as DO concentration decreased towards the substratum and formed a distinctive "belt." This was even more obvious for the simplified biofilm structure (see Figure 4f).

The Influence of Flow Velocity, DO and Biomass Density on COD Fluxes

The model was also used to investigate the influence of flow velocity, substrate concentration and biomass density on COD fluxes and mass transfer properties. COD fluxes were calculated to represent biomass performance. In both, parallel and through flow mode, different combinations of flow velocity (0.001, 0.01, 0.1, 1, and 5 cm/s) and DO concentration (0.01, 0.1, 1, 4, and 8 mg/L) were tested. The relative velocity between the liquid and the carriers estimated based on tracer experiments (videos attached in the supplementary material) spanned a wide range of 0.5–4.8 cm/s with an average value of 1.5 ± 1.3 cm/s. Thereby, the impact of the biofilm surface structure should be revealed. Additionally, the effect of biomass density was studied.

Table II. Structure parameters for all the geometries used

			Geometry 1	Geometry 2	Simplified
Biofilm area	A	$[mm^2]$	0.98	1.00	0.99
Interface length	L_Γ	[mm]	10.7	10.08	5.32
Roughness coefficient	R'_a	[−]	0.34	0.31	0.23
Surface enlargement	α	[−]	2.50	2.34	1.24

The Parallel Flow Mode

The performances of biofilm with real and simplified geometry in terms of COD fluxes were compared for different flow conditions and DO concentrations. The results are presented in Figure 5a and b. The relative difference of COD fluxes is derived by dividing the absolute difference (see Figure S2) by the COD fluxes of the real geometry. Referring to Figure 5a, under low flow velocity conditions ($u \leq 0.1$ cm/s) the differences are positive, which implies that heterogeneous biofilm geometries had better performance with respect to COD fluxes from liquid into the biofilm. However, the difference is low (less than 5%). The negative differences for flow velocities higher than 0.1 cm/s indicate that the flat biofilm had better performance (up to 20 %) than biofilms with heterogeneous structure. Similar results were derived at biomass density of $30{,}000\ g/m^3$ (see Fig. 5b).

It is clear that at same DO concentration, the higher the flow velocity was, the larger the difference in COD flux between the rough and the flat biofilm became. Meanwhile, at the same flow velocity, the higher the DO concentration was, the lower the difference in COD flux. For example in Figure 5a, at $u = 5$ cm/s and low biomass density, the difference was as high as 19 % at a DO concentration of 0.01 mg/L. It decreased to 8% at the DO concentration of 8 mg/L.

To illustrate the variation in the relative difference in COD fluxes presented in Figure 5a and b, the dominance of diffusive and

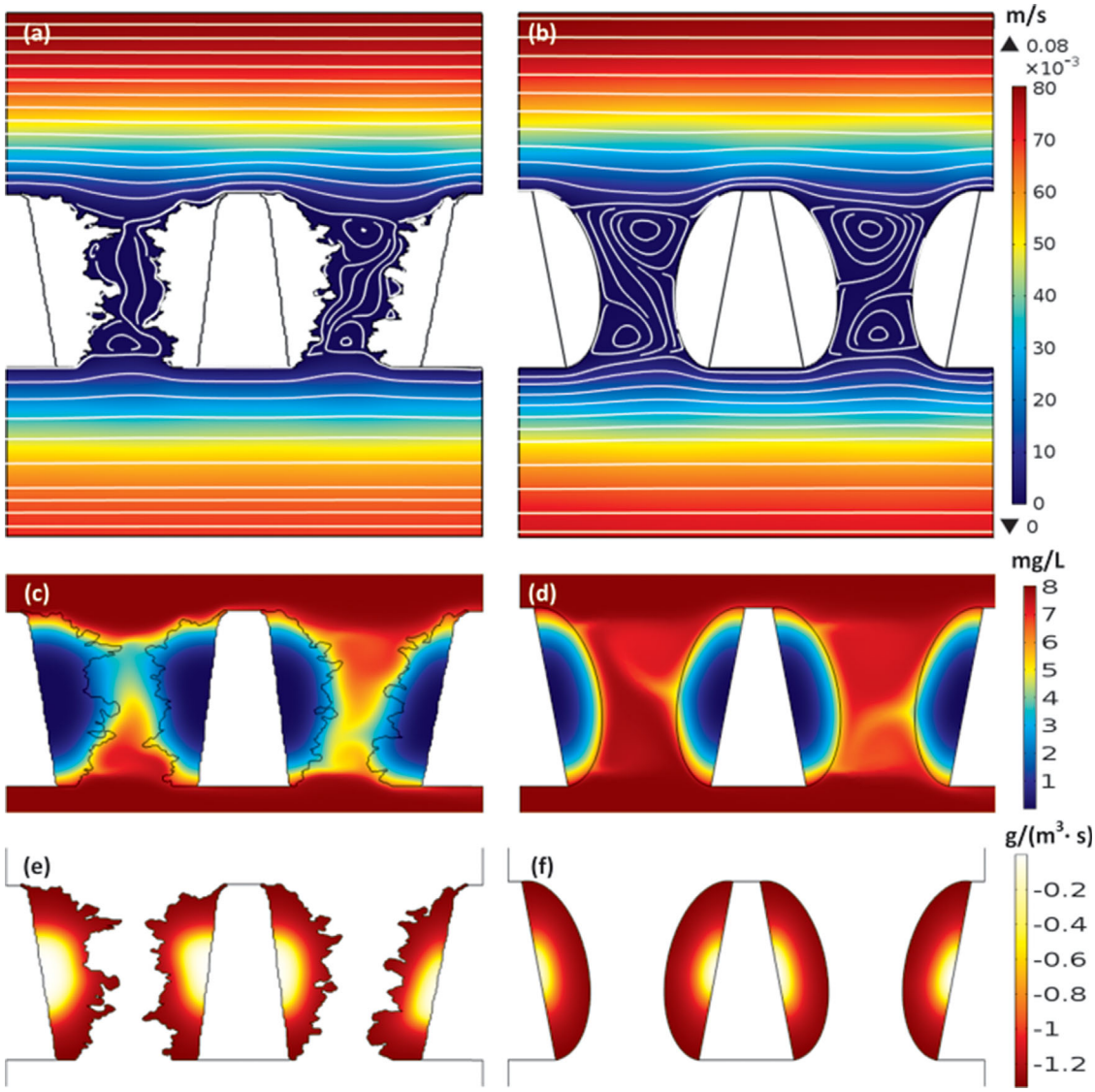

Figure 4. Simulated flow field (**a**) geometry 1 and (**b**) flat simplified biofilm structure, DO concentration field (**c**) and (**d**), and COD removal activity map (**e**) and (**f**) for real and simplified geometry, respectively, with biomass concentration of 15,000 $g \cdot m^{-3}$. The streamlines in (**a**) and (**b**) indicate flow direction. The liquid flows from left to right under laminar flow condition with an inflow velocity of $u = 0.05\ cm \cdot s^{-1}$. To get a closer look at the interaction between biofilm structure and fluid flow, the images for DO concentration field and the activity map were cropped to the most interesting part around biofilm and the carrier surface. DO concentration in the inflow equals 8 $mg \cdot L^{-1}$. COD removal rate has a dimension of $g \cdot m^{-3} \cdot d^{-1}$. The negative values indicate consumption of COD. The figures have a dimension of $2.8 \times 1.4\ mm^2$.

convective mass transport in the simulation domain was compared according to Equations 9 and 10. As an example, the results for DO = 8 mg/L under different flow velocities are plotted in Figure 6 for both the real (G1) and simplified geometry. The color scale shows where the convective transport dominates, while the gray scale indicates where diffusive transport is higher than convective transport. Seen from Figure 6a and b, at low flow velocity, diffusion was the dominant transport mechanism in the whole simulation domain. With increasing flow velocity, convective transport became more and more important compared to diffusive transport. As flow increased, areas of diffusion dominance shrank, and the area of convection dominance expanded. At u = 0.1 cm/s diffusion still prevailed inside the carrier compartments. However, seeing from Figure 6e and f, the transport of substrates in the liquid outside of the compartments was taken over by convection. At u = 1 cm/s in Figure 6h, the compartments with the flat geometry became dominated by convection, but not the compartment with real geometry. At u = 5 cm/s, convective transport dominated the whole liquid domain (Fig. 6i and j).

To characterize mass transfer in the simulation domain, $\overline{Sh}$ were calculated and are summarized in Table III. For the real geometry, at a DO concentration, for example, 0.01 mg/L, $\overline{Sh}$ increased from 1.84 to 27.5 with flow velocity increasing from 0.001cm/s to 5 cm/s. The same trend was also observed for the flat geometry: $\overline{Sh}$ increased

from 3.8 to 69.4 when flow velocity increased from 0.001 to 5 cm/s at DO = 0.01 mg/L. However, at a given flow velocity there existed only a minor variation of $\overline{Sh}$ even with a hundred-fold increase in DO (0.01–1 mg/L). At same DO and flow velocity, $\overline{Sh}$ for the flat geometry was around twice of that for the real geometry, for example, 3.8 and 1.8 for the flat and real geometry, respectively, at u = 0.001 cm/s and DO = 0.01 mg/L.

The Flow Through Mode

To verify how biofilm surface heterogeneity may influence biofilm performance in terms of COD flux, different flow through scenarios were tested. A maximum velocity of 2 cm/s was assumed. The flow velocities investigated included 0.0005, 0.001, 0.01, 0.1, 1, and 2 cm/s. DO concentrations and biomass densities were the same as in the parallel flow cases.

Similar to the parallel flow cases, COD fluxes at the biofilm surfaces for the real and smooth geometries were compared. The results (relative difference) are plotted in Figure 5c and d. For both low (15,000 g/m^3) and high (30,000 g/m^3) biomass density, the differences were generally positive. There was a minor difference in COD flux between the two geometries at u $\leq$ 0.01cm/s. A sharp rise appeared when the flow velocity increased from 0.001 to 0.01cm/s. At the same flow velocity, the difference became smaller with increasing DO concentration. At a given DO concentration, the relative differences in COD flux generally increased with rising flow velocity. The maximum difference of 19% and 20% were reached at u = 2 cm/s and DO = 0.01 mg/L for low and high biomass densities, respectively.

The diffusion-convection plots for the flow through mode are presented in Figure 7. At very low flow velocity (0.0005 cm/s), the domain was dominated by diffusion for both the real and smooth geometry. As flow rate increased, convection started to play a role, see Figure 7d. The prevalence of convection in the domain started already at u = 0.01 cm/s for the flat biofilm. While for the real biofilm structure it was one magnitude higher at u = 0.1 cm/s. From this velocity onwards the whole liquid domain is characterized by convective transport.

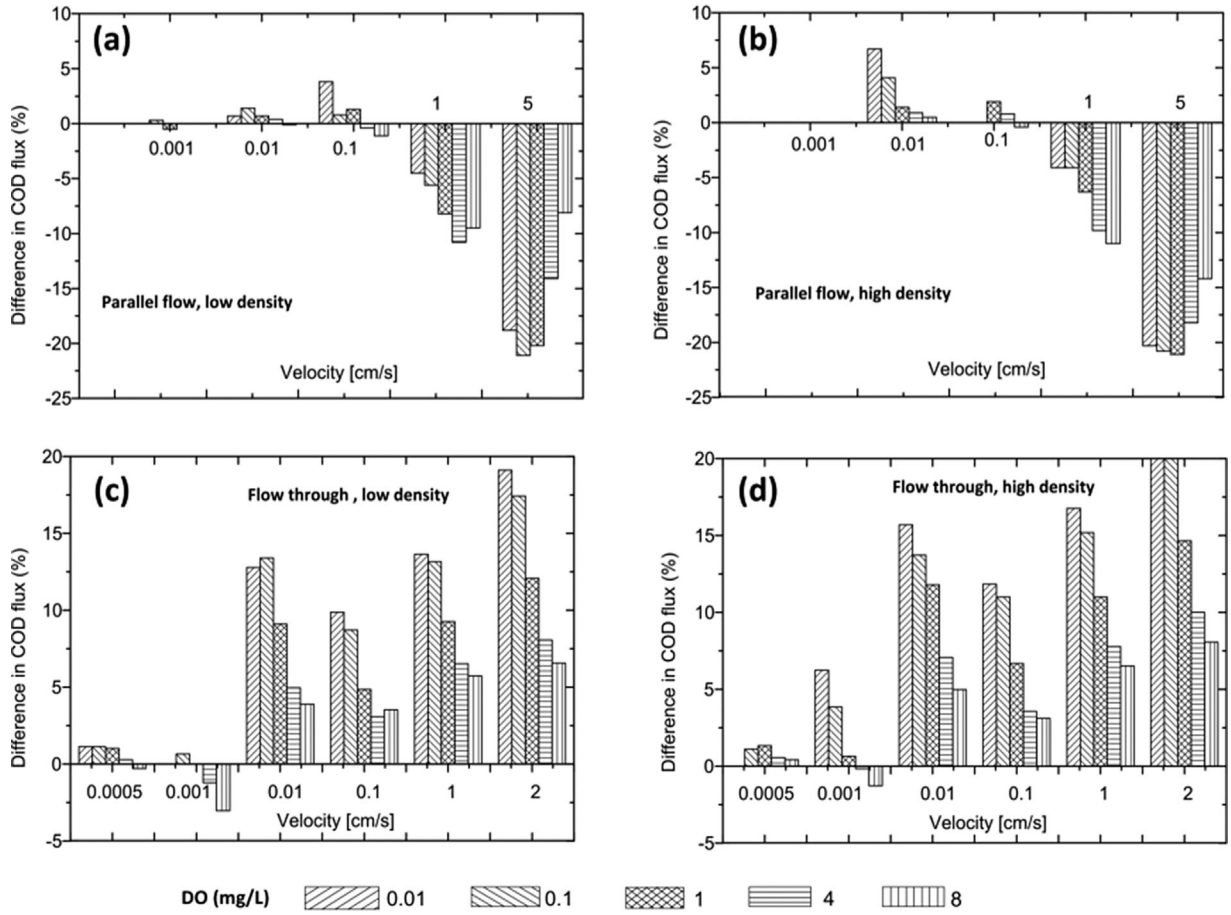

Figure 5. Relative difference in COD flux between the real (G1) and simplified geometries under differentflow and substrate concentration conditions for parallel flow (**a** and **b**) and through flow (**c** and **d**) at low (15,000 g·m^{-3}, (**a** and **c**) and high (30,000 g·m^{-3}, (**b** and **d**) biomass density. In (**d**) the maximum difference at DO of 0.01 and 0.1 mg·L^{-1} is exactly 20%. Positive values indicate higher COD flux for the real geometry over the simplified geometry. Negative values suggest lower COD flux for the real geometry. All the simulations were conducted with same COD concentration (148 mg·L^{-1}) in the inflow.

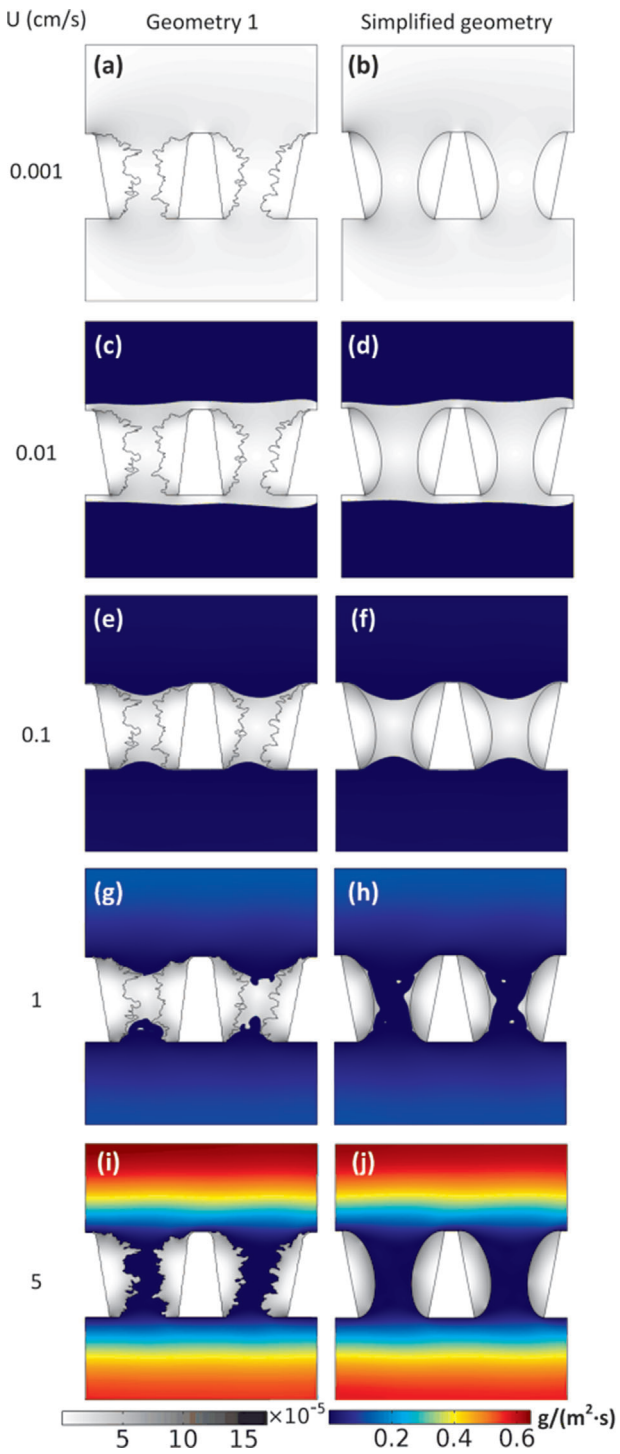

Figure 6. Transition from diffusion to convection dominated mass transport at DO 8 mg·L^{-1} for parallel flow conditions. The gray scale represents the dominance of diffusion at a magnitude of 10^{-5} g·m^{-2}·s^{-1}. Convection prevails in the colored region. The legend applies for all the subfigures.

Difference in Simulation Results Between G1 and G2

The biofilm area of G1 and G2 are very close, which implies the presence of almost the same amount of biomass. Nevertheless, there was a slight difference in biomass distribution inside the compartments. The length of the interface was also different, with 10.7 mm for G1 and 10.08 mm for G2, respectively.

Table III. Spatial averaged Sherwood number calculated for G1 under different flow and substrates conditions for low biomass density and the parallel flow conditions (15,000 g/m^3).

DO (mg/L)	u (cm/s)	0.001	0.01	0.1	1	5
0.01	Real	1.8	3.5	7.2	15.6	27.5
	Simplified	3.8	7.1	14.4	33.0	69.4
0.1	Real	1.8	3.5	7.2	15.6	27.5
	Simplified	3.7	7.1	14.4	33.0	69.5
1	Real	1.8	3.5	7.3	15.6	26.7
	Simplified	3.7	7.1	14.6	33.3	69.7
4	Real	1.8	3.5	7.5	15.1	25.5
	Simplified	3.7	7.1	14.7	33.2	68.9
8	Real	1.8	3.5	7.1	14.8	24.8
	Simplified	3.7	7.1	14.6	33.0	68.3

To reveal the impact of the differences in biofilm structure between G1 and G2, similar simulations were implemented for G2, with DO = 8 mg/L, u = 5 cm/s and u = 2 cm/s for the parallel and flow through mode, respectively. The flow velocity field and substrate distribution in the compartments were mapped and compared to those derived from simulations with G1. The results are presented in Figure 8. In Figure 8a, flow circulated inside the compartments, whereas in Figure 8b water could flow through the compartment (see the streamlines). The effect of the flow pattern on the substrate distribution is shown in Figure 8c and d. Given the same inflow conditions, stagnant zones formed inside the compartments of G1, shown in light green color. Red color prevails in Figure 8d, which suggests no formation of stagnant zones. In the flow through mode, it was clear that the presence of biomass could divert the liquid into different directions, thereby changing the flow field.

In addition to the qualitative visualization of the differences in hydrodynamics, their corresponding performance with respect to COD fluxes were also compared quantitatively and are listed in Table IV, as well as the $\overline{Sh}$ and pressure drop (ΔP) between the inlet and outlet boundary for all the three geometries.

G2 achieved an 11% (low density) and 16% (high density) higher COD flux than G1 under parallel flow conditions. This difference diminished to 2% when water flew through the compartments. Substantial disparity in $\overline{Sh}$ existed between G1 and G2. In the parallel flow cases, $\overline{Sh}$ for G2 was 46, while it was only 25 for G1, both lower than $\overline{Sh}$ of 68 for the simplified biofilm geometry. In the through flow cases, $\overline{Sh}$ was 104 for G1 and 133 for G2, both of which were far lower than that for the flat biofilm with $\overline{Sh}$ of 193. In accordance to $\overline{Sh}$, ΔP also showed the same trend of decrease with the decreasing roughness coefficient from G1 to the flat geometry.

Discussion

The Applicability of Combining Biofilm Imaging and Modeling

The results from the combination of biofilm imaging and modeling demonstrated the capability of this method to incorporate real heterogeneous physical structure of biofilms into mathematical models. In the study of Picioreanu et al. (2000) that investigated the

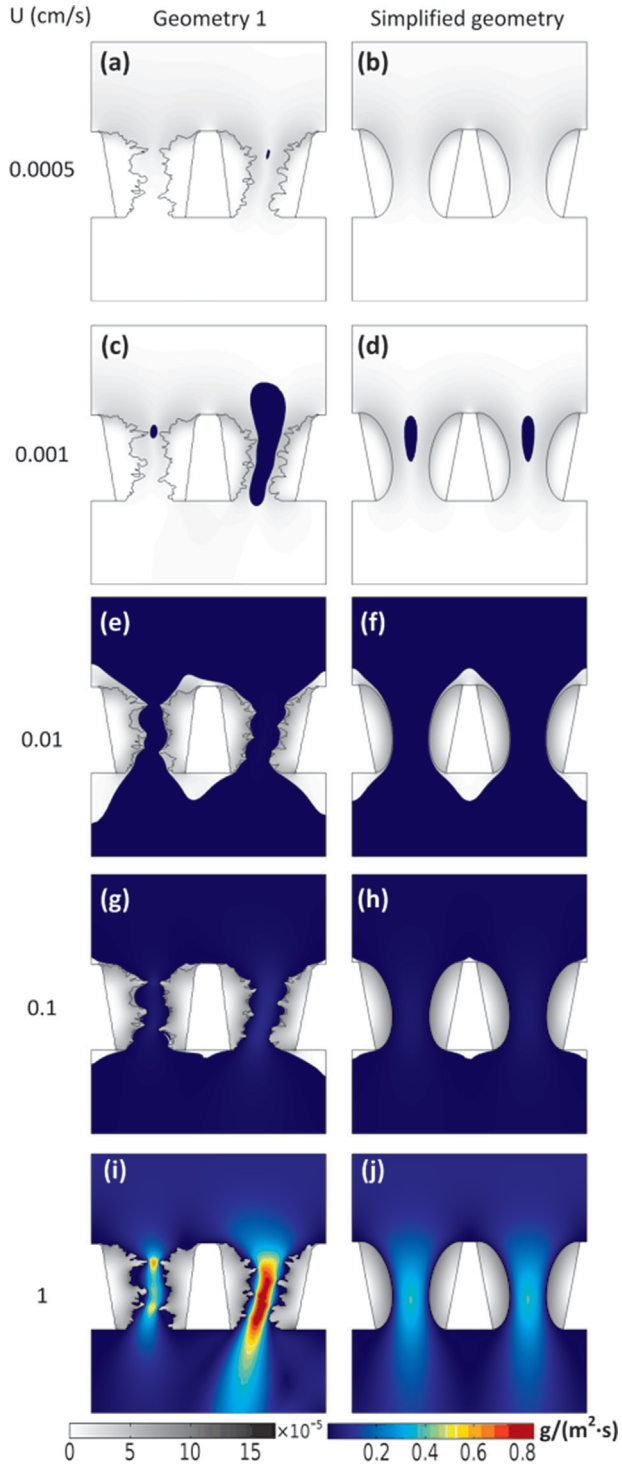

Figure 7. Transition from diffusion to convection dominated mass transport from low to high flow velocity at DO of 8 mg·L^{-1} for flow through conditions. The gray scale represents the dominance of diffusion at a magnitude of 10^{-5} g·m^{-2}·s^{-1}. Convection prevails in the colored region. The legend applies for all the subfigures.

influence of biofilm surface roughness on mass transfer, artificial geometries had to be generated. Böl et al. (2009) and Limbert et al. (2013) used CLSM images to examine the mechanical properties of biofilms. Compared to OCT, the biofilm structure obtained with CLSM may be not representative due to the small field of view as well as the limitation in staining efficiency (Wagner et al., 2010). OCT can provide more representative biofilm structure at the meso-scale that is more relevant for mass transfer (Milferstedt et al., 2009).

Such an approach is not restricted to the MBBR system, and can also be applied in membrane filtration, biofilm studies in water distribution systems as well as to study the mechanical properties of biofilms. In membrane filtration systems, the effect of fouling layers on the membrane surface on the permeability can be investigated, such as done in Martin et al. (2014). In the study of Shen et al. (2015), cross-sectional OCT images were used to simulate the attachment of pathogens onto the surface of a drinking water biofilm. The biofilm structures obtained in the study of Dreszer et al. (2014) who investigated the biofilm formation in membrane filtration processes, can be combined with the modeling approach. On the one hand, it can inspect the influence of biofilm structure on permeate flux and pressure drop. On the other hand, it can help to gain knowledge on the mechanism how biofilm responds to compaction and decompaction. Blauert et al. (2015) investigated the time-resolved deformation of biofilms subjected to fluid shear stress using OCT and estimated the rheological properties of biofilms. The structures acquired in their study can also be taken as structural template to impose mathematical description of the deformation, which would allow deeper mechanistic understanding of the deformation process.

This method can be extended further to incorporate, for example, information on microbial composition obtained from other imaging techniques as well. This can improve the model's accuracy by providing more realistic input, which otherwise often assumes to have homogeneous distribution of the microbial species throughout the biofilm matrix. This is particularly helpful when the interaction among different species is of interest.

The Influence of Biofilm Structure on Local Hydrodynamics and Mass Transfer

Our model allowed for a detailed description of the hydrodynamics at the micro- and meso-scale, which is otherwise difficult to measure. It also showed that slight differences in biofilm structure led to significant differences in local hydrodynamics and thereby mass transfer characteristics. This can be seen qualitatively in Figure 4c and d for the difference between G1 and the smooth geometry and in Figure 8c, d, e, and f for the difference between G1 and G2. This is in agreement with the measurement with MRI by Herrling et al. (2014) showing that the uneven distribution of biomass in different compartments of a biofilm carrier resulted in uneven distribution of liquid flowing through the corresponding compartments. Therefore, capturing biofilm structure as precise as possible is of critical importance when such detailed analysis at the micro- and meso-scale is required.

Comparison of COD fluxes under different flow conditions revealed that the impact of biofilm surface roughness depended strongly on the flow conditions and the relative dominance of diffusive and convective mass transfer. Under the condition of pure diffusion domination, such as at $u \leq 0.1$ cm/s for the parallel flow (see Fig. 6) and $u \leq 0.001$ cm/s for the flow through mode (see Fig. 7), the rough biofilm had slightly higher COD flux than the

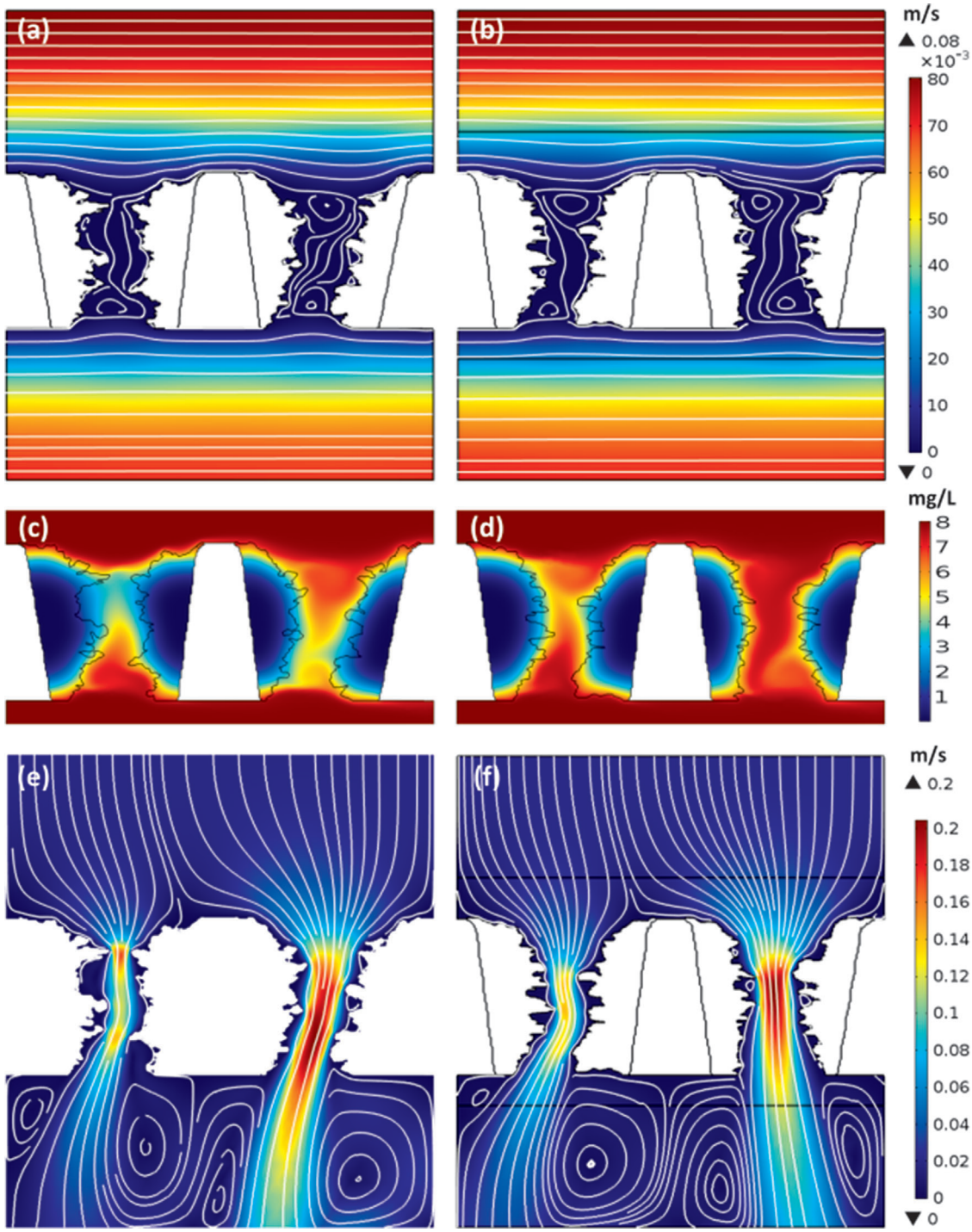

Figure 8. Flow field in parallel (**a** and **b**) and through flow mode (**e** and **f**) and DO concentration fieldsimulated in parallel flow mode with G1 (left) and G2 (right).

smooth biofilm. Under the condition of weak external mass transfer, the increased R'_a from the smooth geometry to 0.34 for G1 provided the rough geometry with more L_Γ (100% more), thereby more contact to substrate. For the parallel flow cases, the transition from diffusion to convection dominance inside the compartments led to better performance of the smooth biofilm. This is similar to the findings of Picioreanu et al. (2000) who concluded that rough biofilm structure led to decreased conversion rates in the range of flow velocity simulated in their study. However, due to stability and accuracy issues, biofilm behavior at high flow velocity was not simulated in Picioreanu et al. (2000). In our case, as liquid was forced to flow through the compartments, resulting in maximum flow velocity up to $u = 20$ cm/s in the compartments (see Fig. 8e), the dominance of convective transport above biofilm surface

Table IV. Comparison of COD fluxes (g/(m^2 · d)),$\bar{Sh}$ and pressure drop (Pa) among the different simulations with different biofilm geometries.

	Parallel flow (u = 5 cm/s)			Flow through (u = 2 cm/s)		
	G1	G2	Simplified	G1	G2	Simplified
COD						
Low biofilm density	20.4	22.8	22.0	25.6	26.3	23.9
High biofilm density	27.9	32.4	31.8	40.4	40.9	37.2
$\bar{Sh}$						
—	24.8	41.8	68.3	103.5	132.9	192.7
ΔP						
—	0.87	0.75	0.53	37.4	30.6	5.6

rendered the whole biofilm surface to be active and contributed to substrate conversion. Therefore, the rough biofilm appeared to be advantageous over the smooth biofilm. Moreover, at this high flow velocity the small biofilm branches tend to oscillate (not included in the current simulation), which might increase the mass transfer further (Taherzadeh et al., 2012). For the counter-diffusion biofilms, Pavissich et al. (2014) also observed lower conversion rates at low flow velocity in the rougher biofilm structure and higher rates at higher velocities. Nevertheless, in co- and counter-diffusional biofilms, the effect of biofilm surface roughness can be different, as has been pointed out by Pavissich et al. (2014) and needs to be investigated further.

Quantification of mass transfer through $\overline{Sh}$, presented in Table III, shows that $\overline{Sh}$ improved with increasing flow velocity. The increase of $\overline{Sh}$ does lead to a linear increase in biofilm activity (Wäsche et al., 2002). This can be clearly seen in Table IV, $\overline{Sh}$ increased about three folds with decreasing R'_a, while COD flux increased only by about 10%. At high flow velocity thereby high $\overline{Sh}$, the biofilm activity is not limited by mass transfer, rather by biomass density. Therefore, doubling of biomass density increased the COD flux significantly. We have to admit that this is only valid by assuming the same diffusion coefficients in dense and less dense biofilms. More accurate study on the topic requires better understanding of the reactor scale hydrodynamics (Boltz and Daigger, 2010).

As a first step, only 2D biofilm images were used in the current study, similar to the study of Pavissich et al. (2014) and Martin et al. (2014), despite the capability of OCT in acquiring 3D biofilm structure. Further extension of the method into importing 3D biofilm structure would improve the description of the local hydrodynamics.

Conclusions

The method developed in this study provides the opportunity to combine detailed biofilm structure obtained from biofilm imaging at the meso-scale by means of OCT and biofilm modeling to enhance our understanding of the hydrodynamics and mass transfer processes at the meso-scale. The simulation results with different geometries revealed that:

- The approach of incorporating a real biofilm structure into a mathematical simulation allowed for the detailed description of local hydrodynamics and mass transfer characteristics at the meso-scale.
- Depending on the flow conditions, the heterogeneous geometry may behave different than the smooth biofilms with respect to substrate flux. Under the condition of pure diffusive mass transfer, rough biofilms appeared to show higher mass transfer flux due to the large liquid-biofilm interface providing more contact to substrates. Rough biofilms also resulted in higher mass transfer fluxes than smooth biofilms with enhanced mass transfer at biofilm surface under flow through conditions.
- The low difference in COD flux between the rough and smooth geometry under parallel flow conditions imply that assuming smooth biofilm geometry can derive satisfying results for the design of MBBRs.

The authors acknowledge the support of AnoxKaldnes. Financial support from the Water Science Alliance of The Helmholtz Association is also acknowledged.

Nomenclature

R'_a	roughness coefficient
α	surface enlargement factor
u	velocity field
D_i	diffusion coefficient of substrate *i*
S_i	concentration of substrate *i*
J	substrate flux
J_c	local convective flux
J_D	local diffusive flux
Sh	Sherwood number
$\bar{Sh}$	spatially averaged Sherwood number
$L_{f,i}$	local biofilm thickness at point *i*
$\bar{L}_f$	average biofilm thickness
L_h	characteristic length for the calculation of *Sh*
L_Γ	length of the biofilm–liquid interface
L_s	length of the substratum
r_i	turnover rate of substrate *i*
Y_H	yield coefficient of heterotrophic bacteria
X_H	concentration of heterotrophic organism in the biofilm
μ_H	maximum specific growth rate of X_H
p	pressure
μ	dynamic viscosity of water
x	x direction of the simulation domain
y	y direction of the simulation domain

References

Alpkvist E, Klapper I. 2007. A multidimensional multispecies continuum model for heterogeneous biofilm development. Bull Math Biol 69(2):765–789.

Blauert F, Horn H, Wagner M. 2015. Time-resolved biofilm deformation measurements using optical coherence tomography. Biotechnol Bioeng 112(9):1893–1905.

Böl M, Möhle RB, Haesner M, Neu TR, Horn H, Krull R. 2009. 3D finite element model of biofilm detachment using real biofilm structures from CLSM data. Biotechnol Bioeng 103(1):177–186.

Boltz JP, Daigger GT. 2010. Uncertainty in bulk-liquid hydrodynamics and biofilm dynamics creates uncertainties in biofilm reactor design. Water Sci Technol 61(2):307.

Derlon N, Peter-Varbanets M, Scheidegger A, Pronk W, Morgenroth E. 2012. Predation influences the structure of biofilm developed on ultrafiltration membranes. Water Res 46(10):3323–3333.

Dreszer C, Wexler AD, Drusová S, Overdijk T, Zwijnenburg A, Flemming H, Kruithof JC, Vrouwenvelder JS. 2014. In-situ biofilm characterization in membrane systems using optical coherence tomography: Formation, structure, detachment and impact of flux change. Water Res 67:243–254.

Eberl H, Picioreanu C, Heijnen J, van Loosdrecht M. 2000. A three-dimensional numerical study on the correlation of spatial structure, hydrodynamic conditions, and mass transfer and conversion in biofilms. Chem Eng Sci 55(24):6209–6222.

Henze M. 2000. Activated sludge models ASM1 ASM2 ASM2d and ASM3. London: IWA Pub. vi, p 121.

Herrling MP, Guthausen G, Wagner M, Lackner S, Horn H. 2014. Determining the flow regime in a biofilm carrier by means of magnetic resonance imaging. Biotechnol Bioeng 112(5):1023–1032.

Horn H, Lackner S. 2014. Modeling of biofilm systems: A review. Adv Biochem Eng Biotechnol 146:53–76.

Horn H, Morgenroth E. 2006. Transport of oxygen, sodium chloride, and sodium nitrate in biofilms. Chem Eng Sci 61(5):1347–1356.

Huang D, Swanson E, Lin C, Schuman J, Stinson W, Chang W, Hee M, Flotte T, Gregory K, Puliafito C. 1991. Optical coherence tomography. Science 254(5035): 1178–1181.

Ivleva NP, Wagner M, Horn H, Niessner R, Haisch C. 2009. Towards a nondestructive chemical characterization of biofilm matrix by Raman microscopy. Anal Bioanal Chem 393(1):197–206.

Janjaroen D, Ling F, Monroy G, Derlon N, Mogenroth E, Boppart SA, Liu W, Nguyen TH. 2013. Roles of ionic strength and biofilm roughness on adhesion kinetics of *Escherichia coli* onto groundwater biofilm grown on PVC surfaces. Water Res 47(7):2531–2542.

Kreft JU, Picioreanu C, Wimpenny JW, van, Loosdrecht, MCM. 2001. Individual-based modelling of biofilms. Microbiology 147(11):2897–2912.

Laspidou CS, Rittmann BE. 2004. Evaluating trends in biofilm density using the UMCCA model. Water Res 38(14–15):3362–3372.

Lawrence JR, Neu TR. 1999. Confocal laser scanning microscopy for analysis of microbial biofilms. In: Biofilms Elsevier. p 131-144.

Lide, David R. (Hg.) 2003: CRC handbook of chemistry and physics. A ready-reference book of chemical and physical data, 84th ed. Boca Raton: CRC Press.

Limbert G, Bryan R, Cotton R, Young P, Hall-Stoodley L, Kathju S, Stoodley P. 2013. On the mechanics of bacterial biofilms on non-dissolvable surgical sutures: A laser scanning confocal microscopy-based finite element study. Acta Biomater 9(5):6641–6652.

Manz B, Volke F, Goll D, Horn H. 2003. Measuring local flow velocities and biofilm structure in biofilm systems with Magnetic Resonance Imaging (MRI). Biotechnol Bioeng 84(4):424–432.

Martin KJ, Bolster D, Derlon N, Morgenroth E, Nerenberg R. 2014. Effect of fouling layer spatial distribution on permeate flux: A theoretical and experimental study. J Membr Sci 471:130–137.

Milferstedt K, Pons M, Morgenroth E. 2009. Analyzing characteristic length scales in biofilm structures. Biotechnol Bioeng 102(2):368–379.

Murga R, Stewart PS, Daly D. 1995. Quantitative analysis of biofilm thickness variability. Biotechnol Bioeng 45(6):503–510.

Pavissich JP, Aybar M, Martin KJ, Nerenberg R. 2014. A methodology to assess the effects of biofilm roughness on substrate fluxes using image analysis, substrate profiling, and mathematical modelling. Water Sci Technol 69(9):1932–1941.

Picioreanu C, Kreft J, van Loosdrecht MCM. 2004. Particle-based multidimensional multispecies biofilm model. Appl Environ Microbiol 70(5):3024–3040.

Picioreanu C, van Loosdrecht MCM, Heijnen J. 1998. Mathematical modeling of biofilm structure with a hybrid differential-discrete cellular automaton approach. Biotechnol Bioeng 58(1):101–116.

Picioreanu C, van Loosdrecht MC, Heijnen JJ. 2000. A theoretical study on the effect of surface roughness on mass transport and transformation in biofilms. Biotechnol Bioeng 68(4):355–369.

Schindelin J, Arganda-Carreras I, Frise E, Kaynig V, Longair M, Pietzsch T, Preibisch S, Rueden C, Saalfeld S, Schmid B, Tinevez J, White DJ, Hartenstein V, Eliceiri K, Tomancak P, Cardona A. 2012. Fiji: An open-source platform for biological-image analysis. Nat Methods 9(7):676–682.

Shen Y, Monroy G, Derlon N, Janjaroen D, Huang C, Morgenroh E, Boppart S, Ashbolt N, Liu W, Nguyen T. 2015. Role of biofilm roughness and hydrodynamic conditions in *Legionella pneumophila* adhesion to and detachment from simulated drinking water biofilms. Environ Sci Technol 49(7): 4274–4282.

Stewart PS. 2003. Diffusion in biofilms. J Bacteriol 185(5):1485–1491.

Taherzadeh D, Picioreanu C, Horn H. 2012. Mass transfer enhancement in moving biofilm structures. Biophys J 102(7):1483–1492.

Wagner M, Taherzadeh D, Haisch C, Horn H. 2010. Investigation of the mesoscale structure and volumetric features of biofilms using optical coherence tomography. Biotechnol Bioeng 107(5):844–853.

Wanner O, Reichert P. 1996. Mathematical modeling of mixed-culture biofilms. Biotechnol Bioeng 49:172–184.

Wäsche S, Horn H, Hempel DC. 2002. Influence of growth conditions on biofilm development and mass transfer at the bulk/biofilm interface. Water Res 36(19): 4775–4784.

Xi C, Marks D, Schlachter S, Luo W, Boppart SA. 2006. High-resolution three-dimensional imaging of biofilm development using optical coherence tomography. J Biomed Opt 11(3):34001.

Yang X, Beyenal H, Harkin G, Lewandowski Z. 2001. Evaluation of biofilm image thresholding methods. Water Res 35:1149–1157.

Supporting Information

Additional supporting information may be found in the online version of this article at the publisher's web-site.